Showcasing research from Professor Tae Joo Park's laboratory, Department of Materials and Chemical Engineering, Hanyang University, Ansan, Republic of Korea.

Advanced atomic layer deposition (ALD): controlling the reaction kinetics and nucleation of metal thin films using electric-potential-assisted ALD

Electric potential assisted ALD was demonstrated for Ru film growth. The surface reaction was modified by electric potential, which affected the nucleation and microstructure. Assorted film properties were highly improved.

As featured in:

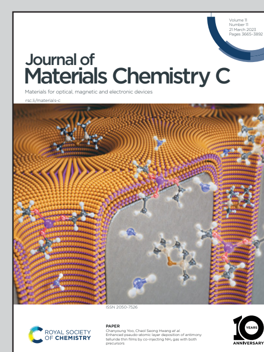

See Woo-Hee Kim, Ji-Hoon Ahn, Tae Joo Park *et al.*, *J. Mater. Chem. C*, 2023, **11**, 3743.

ROYAL SOCIETY OF CHEMISTRY

rsc.li/materials-c

Registered charity number: 207890

Journal of
Materials Chemistry C

ROYAL SOCIETY OF CHEMISTRY

PAPER

View Article Online
View Journal | View Issue

Published on 20 February 2023. Downloaded by Hanyang University on 4/15/2024 2:29:21 AM.

Cite this: *J. Mater. Chem. C*, 2023, 11, 3743

Advanced atomic layer deposition (ALD): controlling the reaction kinetics and nucleation of metal thin films using electric-potential-assisted ALD†

Ji Won Han, ‡[a] Hyun Soo Jin,‡[ab] Yoon Jeong Kim,[a] Ji Sun Heo,[a] Woo-Hee Kim, *[a] Ji-Hoon Ahn *[a] and Tae Joo Park *[a]

Received 8th November 2022,
Accepted 20th February 2023

DOI: 10.1039/d2tc04755a

rsc.li/materials-c

Ru thin films are grown using electric-potential-assisted ALD (EA-ALD), modifying the thin film growth behavior with an electric potential applied to the substrate. The generated electric field increases the (adsorption) rate of the precursor molecules onto the substrate, and thus the Ru nucleation density. As a result, the grain size and critical thickness for a continuous film decreases. In addition, the electric potential modifies the bonding energy of surface functional groups, which crucially affects the film growth behavior *via*, for example, the crystal orientation, grain size, and physical density. A negative bias decreases the surface Ru–O bonding strength, which enhances the surface reaction with the precursor molecules promoting the grain growth. However, a positive bias increases the surface Ru–O bonding strength, which impedes the grain growth resulting in small and uniform grains. Even though EA-ALD induces a higher oxygen concentration in the film due to the smaller size of the grains, the physical density of the film is higher. Consequently, an ultrathin (∼3 nm) and continuous Ru film with a low resistivity (∼40 μΩ cm) and a high effective work function (∼5.1 eV) is obtained.

Introduction

The scaling of three-dimensional semiconductor devices such as fin-field effect transistors (FinFETs) and gate-all-around FETs has been accelerated, and thus the structural complexity of the devices has rapidly increased.[1–3] Therefore, the demand for techniques that can achieve ultrathin and uniform metal thin film deposition has grown, and the atomic layer deposition (ALD) technique, which provides good conformality of the film even on complicated structures, has been widely adopted. However, the ALD of a metal film on Si and various oxide substrates exhibits island growth behavior due to the high surface energy of the metal,[4–6] and thus the critical thickness, which is the minimum thickness for coalescence of the islands to form a continuous metal film, is relatively high. Therefore, this phenomenon needs to be overcome whilst maintaining the resistivity and physical properties (such as the physical density and the surface roughness) of the film.[7–10] Until now, however, the solution to this problem has focused mainly on the development of new precursors.

Meanwhile, Ru is known for having physical, chemical, and electrical properties that meet the requirements for next-generation semiconductor devices.[7,8] Therefore, it has been considered as a promising electrode material for dynamic random-access memory (DRAM), metal–oxide–semiconductor FETs (MOSFETs), and back-end-of-line metallization.[11–15]

In this study, the growth of high-quality ultrathin and uniform Ru films is demonstrated using electric-potential-assisted ALD (EA-ALD), which is a novel ALD process assisted by an electric potential applied on the substrate, thus generating an electric field enhancing the surface adsorption of precursor molecules and surface potential, modifying the bonding strength of the surface functional groups. The increased impingement (adsorption) rate of the precursor molecules by the electric field increases the nucleation density during the initial stage of growth and, thus, the critical thickness is reduced. The applied electric potential controls the surface reaction kinetics and nucleation behavior through modification of the bonding strength of the surface groups. As a result, the microstructure and chemical composition of the Ru film are improved, resulting in Ru films with a low resistivity and a high effective work function at ultrathin (∼3 nm) thicknesses.

[a] *Department of Materials Science and Chemical Engineering, Hanyang University, Ansan 15588, Republic of Korea. E-mail: tjp@hanyang.ac.kr*
[b] *SK Hynix. Inc., 2091, Gyeongchung-daero, Icheon 17336, Republic of Korea*

† Electronic supplementary information (ESI) available: ALD process recipe of control ALD and EA-ALD; AFM line profiles and growth rates of Ru films grown using control ALD and EA-ALD; O 1s core level spectra of Ru films grown using control ALD and EA-ALD; TiN electrode fabrication process for electrical measurements. See DOI: **https://doi.org/10.1039/d2tc04755a**

‡ Ji Won Han and Hyun Soo Jin equally contributed.

Published on 20 February 2023. Downloaded by Hanyang University on 4/15/2024 2:29:21 AM.

Experimental

Film deposition

Ru thin films were grown on a thermally-grown SiO_2 (~300 nm)/p-type Si (boron, 5 × 10^{14} cm^{-3}) substrate using a 6-inch diameter scale traveling-wave-type ALD reactor at 265 °C. The substrate was sonicated for 5 min in acetone, iso-propanol (IPA), and deionized (DI) water, respectively. (Ethylbenzene) (1-ethyl-1,4-cyclohexadiene) ruthenium(0) (EBECHRu, Hansol Chemical) heated at 100 °C in high purity O_2 (99.999%) with a flow rate of 100 standard cubic centimeters per minute (sccm) was used as a precursor and reactant, respectively. High purity N_2 (99.999%) was used as a purge and a carrier gas with a flow rate of 100 sccm.

Microstructure analysis

Thickness and surface morphologies of the thin films were analyzed using atomic force microscopy (AFM; XE-100, Park Systems). AFM specimens for thickness measurements were patterned *via* dry etching using 180 g m^{-3} of O_3 with a flow rate of 500 sccm at 150 °C. Image processing for nucleation density calculations and thickness measurements was conducted using XEI (Park Systems) software. The layer density of the film was measured using X-ray fluorescence spectroscopy (XRF; ARL Quant'X, ThermoFisher Scientific). The crystal structure of the thin film was confirmed using grazing incidence X-ray diffraction (GI-XRD; Smartlab, Rigaku) with an incident angle of 1°. The thickness and morphology of the film were observed using 200 kV field emission transmission electron microscopy (TEM; JEM-2100F, JEOL). TEM specimens were fabricated *via* focused ion beam etching (FIB; Quanta 3D FEG, FEI). The chemical composition and binding state of the film were analyzed using X-ray photoelectron spectroscopy (XPS; Nexsa, ThermoFisher Scientific) with an Al Kα X-ray source and time-of-flight secondary mass spectroscopy (TOF-SIMS; TOF.SIMS 5, ION-TOF).

Electrical measurements

A four-point probe method with the van der Pauw configuration was used to measure the electrical resistivity of the Ru films. Square SiO_2/Si wafer coupons (20 mm × 20 mm) with TiN (100 nm) electrodes at each corner deposited *via* dc magnetron sputtering through a shadow mask were used as the substrate for resistivity measurements using a Hall measurement instrument (HMS-3000, Ecopia).

Metal–oxide–semiconductor (MOS) capacitors were fabricated for work function measurements using a slant SiO_2(300 nm)/p-type Si substrate prepared by wet etching with a dilute hydrogen fluoride solution (HF, 10 wt%). The thickness of the SiO_2 film ranged from 50 to 300 nm. Then, a 20 nm-thick ALD Ru film was grown on the prepared substrate, and a TiN top electrode (100 nm) was formed using dc magnetron sputtering with a shadow mask, which was also used as a hard mask for dry etching of the Ru film at 150 °C using O_3 at a concentration of 180 g m^{-3}. The capacitance–voltage (C–V) characteristics of the MOS capacitors were measured using an E4980A precision LCR meter (Keysight) at a frequency of 1 MHz.

Results and discussion

A schematic of the EA-ALD reactor equipped with a stage connected to DC power supply is shown in Fig. 1a, which enabled the electric potential to be applied to the stage and substrate during the ALD process. For electrical isolation of the stage, an insulating unit was inserted between the stage and the chamber body. All of the chamber body parts (except for the electrically-isolated stage, *i.e.*, the chamber top (lid), chamber wall, and chamber bottom) were grounded during the process. In Fig. 1a, the equipotential surface is indicated as a purple dome, and the electric field generated by the applied electric potential is indicated by blue arrows. Ru films were grown using EA-ALD with an applied voltage of +30 V and −30 V during Ru precursor feeding (denoted as +30 V Ru and −30 V Ru, respectively), and these were compared with control Ru films grown using the conventional ALD process (Fig. S1, ESI†).

To study the growth behavior of the EA-ALD Ru film, using AFM we examined the surface morphology of Ru films during the initial growth (nucleation) stage (10 ALD cycles), as shown in Fig. 1b. The nucleation densities of the films obtained from AFM image analysis were 430, 450 and 500 islands per μm^2 for control Ru, −30 V Ru, and +30 V Ru, respectively. This revealed that EA-ALD increased the nucleation density of the film. Subsequently, the growth behavior of the Ru film after the nucleation stage was then studied by analyzing the layer density of Ru measured using XRF, because the thickness of the ultrathin metal film is difficult to determine due to its island growth nature. Fig. 1c shows the Ru layer density of the film as a function of ALD cycle number. The deposition rate of the films was obtained from the slopes of the curves. A transition point where the deposition rate changed was observed in all the Ru films. The deposition rate for the EA-ALD Ru films was higher than that for the control Ru film over the entire range of the ALD cycle number. Fig. 1d shows a schematic for the cause of the change in the deposition rate (the transition point). The effective surface area is larger during the stage of early growth due to the island growth of the Ru film compared with the subsequent layer-by-layer (LBL) growth stage, and this increased surface area results in the higher deposition rate seen during the island growth stage.[16] In particular, the Ru precursor used in this study, *i.e.*, (ethylbenzene)(1-ethyl-1,4-cyclohexadiene) ruthenium(0) (EBECHRu), is zero-valent and thus advantageous in nucleation,[2,17] which might promote this behavior. The effective surface area then decreased when coalescence began to occur, which decreased the deposition rate. In Fig. 1e, the growth-per-cycle (GPC; ΔRu layer density/ΔALD cycles) was calculated as a function of the number of ALD cycles to clarify the growth transition points. The GPC values of the EA-ALD Ru films were saturated earlier than that of the control Ru film (at 120 ALD cycles for EA-ALD Ru and 150 cycles for control Ru). Puurunen *et al.* reported that this type of

 This journal is © The Royal Society of Chemistry 2023

Published on 20 February 2023. Downloaded by Hanyang University on 4/15/2024 2:29:21 AM.

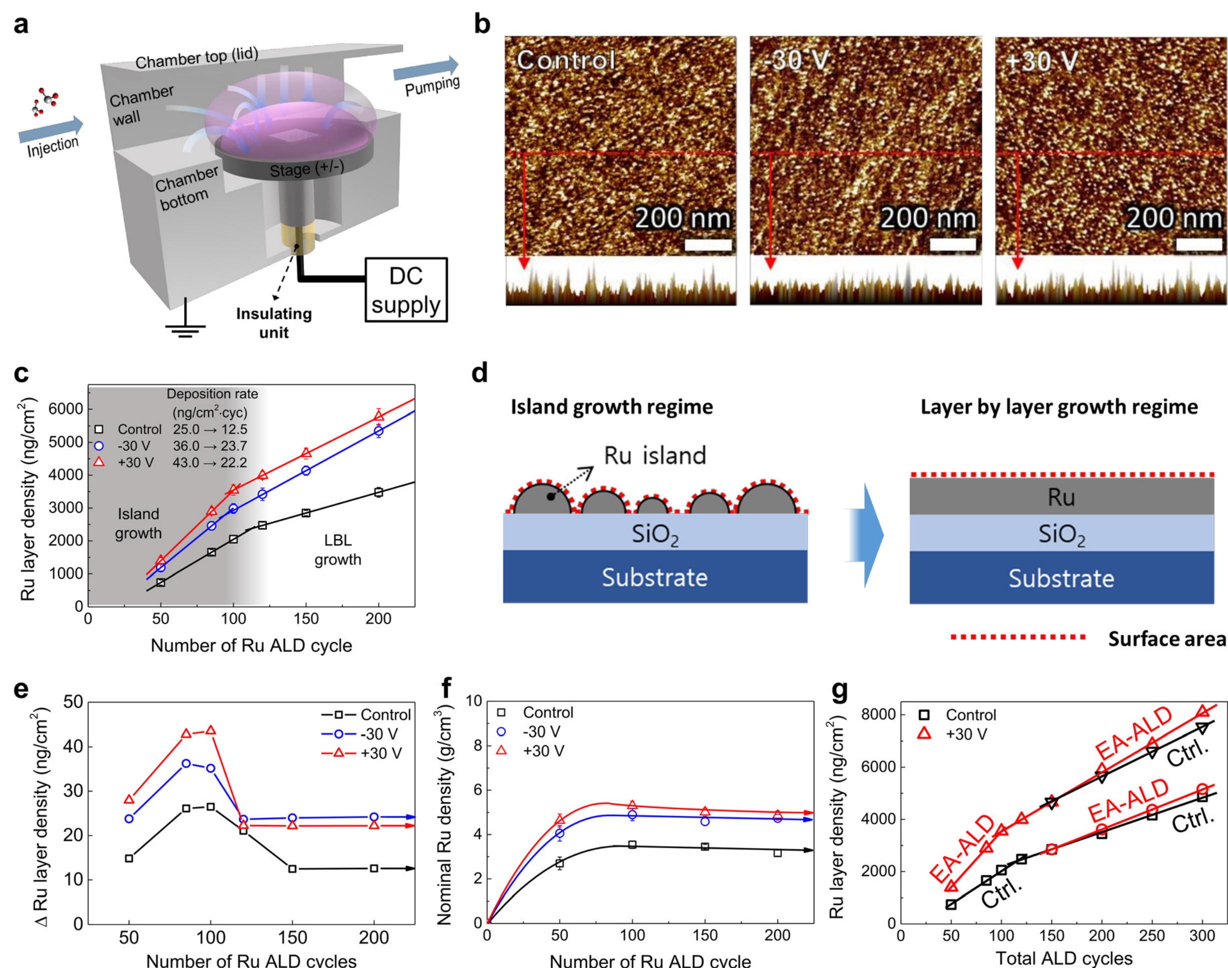

Fig. 1 (a) Schematic of the EA-ALD reactor equipped with a stage connected to a DC power supply. (b) AFM images of the Ru films grown on an SiO_2 substrate using control and EA-ALD with 10 cycles. EA-ALD increased the nucleation density of the film. (c) Ru layer density of the film as a function of the number of ALD cycles. The slope of the curves indicates the Ru deposition rate, which was enhanced for EA-ALD. The earlier growth transition of the EA-ALD films suggests that the critical thickness for a continuous film was reduced. (d) Schematic of the surface area of the Ru films. The effective surface area of the film is larger during the island growth stage than during the subsequent layer-by-layer (LBL) growth stage. (e) Growth per cycle (GPC; ΔRu layer density/ΔALD cycles) and (f) nominal physical density of the Ru films as a function of the number of ALD cycles. (g) Ru layer density of the films grown using consecutive processes of control and EA-ALD. The deposition rate (slope of the curve) of EA-ALD Ru was higher than that of control Ru in both cases.

growth behavior reflected the island growth characteristics, and that the GPC became saturated at the transition point from island growth to LBL growth.[16,18–21] Therefore, we conclude that the critical thickness for a continuous film is reduced using EA-ALD, which is attributed to the increased nucleation density in the EA-ALD film as discussed above.

The enhanced nucleation in EA-ALD is induced by the electric field generated by the applied potential during ALD. The precursor molecules located in the electric field during EA-ALD are aligned to the electric field as a form of induced dipole or polar molecule.[22,23] Precursors are then forcibly drawn toward the substrate where the electric flux density is higher (Fig. 1a).[22,23] Therefore, EA-ALD enhanced the impingement rate to increase the nucleation density of the film. Interestingly, the nucleation densities (Fig. 1b) and the deposition rates (Fig. 1c) of −30 and +30 V Ru were different, even though the electric flux gradient and the induced dipole moment should be identical for both types of EA-ALD. In addition, the deposition rate of +30 V Ru was higher than that of −30 V Ru before the transition point (43 and 36 ng cm^{-2} cycle, respectively), after which it was reversed (22.2 and 24.2 ng cm^{-2} cycle, respectively). Furthermore, in Fig. 1f the nominal Ru density of the films [the Ru layer density measured *via* XRF/thickness measured *via* AFM (Fig. S2, ESI†)] is higher for +30 V Ru than for −30 V Ru, and both of these are higher than that of control Ru. Therefore, we inferred that EA-ALD affected not only the impingement rate but also the surface reaction kinetics, by modifying the electrochemical potential of the surface species during ALD.

To confirm the presence of other factors affecting the film growth behavior in addition to the impingement rate, we deposited heterogeneous Ru films using consecutive processes

Published on 20 February 2023. Downloaded by Hanyang University on 4/15/2024 2:29:21 AM.

of control and EA-ALD. Each control and EA-ALD Ru (+30 V Ru) film was grown to its critical thickness, upon which EA-ALD and control Ru films were then grown, respectively. This excludes the effect from the growth characteristics during the island growth stage, which is crucially affected by the impingement rate. In Fig. 1g, the Ru layer density of the control (black square symbols) and the EA-ALD (red triangle symbols) films was measured as a function of the ALD cycle number. In both cases, the slope of the curves (deposition rate) for EA-ALD Ru is higher than that of the control Ru film. This suggests that the growth behavior of EA-ALD does not result simply from the increased nucleation density *via* the impingement rate.

The mechanism of EA-ALD can be elucidated as described below. Fig. 2a shows schematics of the surface reactions during the ALD of a Ru film. In Ru ALD using oxygen as a reactant, during the precursor feeding step, the ligands of the precursor are removed *via* a combustion reaction with the oxygen in the surface functional groups,[24,25] and subsequently during the reactant feeding step the remaining ligands of the chemisorbed precursor react with the supplied oxygen. Here, we focus on the surface reaction that occurs during the precursor feeding step, as shown in Fig. 2b, because the electric potential for EA-ALD was applied at the precursor feeding step. Surface Ru–O bonds (indicated by the blue box) formed during the oxygen feeding step are replaced by Ru–Ru bonds due to the surface reaction with the incoming precursors (ligand combustion, indicated by the red box),[25,26] which must be accompanied by cleavage of the surface Ru–O bond. Therefore, the surface reaction rate during precursor feeding is crucially affected by the bonding strength of the Ru–O bond.[26] Shaik *et al.* reported that the bonding strength and reaction kinetics of a molecule are affected by an external electric potential or field oriented along with the bonding axis due to induced polarization of the molecular orbital (MO).[27–30] The Ru–O bond has an ionic character in which electrons are transferred from Ru to O.[31,32] In addition, the MO of the Ru–O bond is known to have partially filled π* orbitals (anti-bonding orbitals), as shown in Fig. 2c,[33,34] which weakens the bonding strength as more electrons fill up the orbitals.[35,36] Therefore, the applied positive electric potential deviates the MO toward the Ru, which decreases the electron density in the π* orbital, resulting in an increased Ru–O bond strength. By contrast, a negative electric potential induces an increase in electron density in the π* orbital by deviating the MO toward the O, followed by a decrease in the Ru–O bond strength.

The modified bonding strength of the surface Ru–O group can crucially affect the chemical reaction rate,[27–30] surface energy,[37–49] and surface diffusion,[50–55] resulting in changes in the film growth behavior. Fig. 2d shows the growth behavior of the control and EA-ALD Ru films during the initial growth (island growth) stage. As discussed above, EA-ALD enables modulation of the bonding energy as well as an enhancement of the impingement rate. Considering the bonding energy modulation, the grain size of −30 V Ru is larger than that of control Ru, because the weakened bonding energy of Ru–O by the applied negative potential enhances the chemical adsorption of

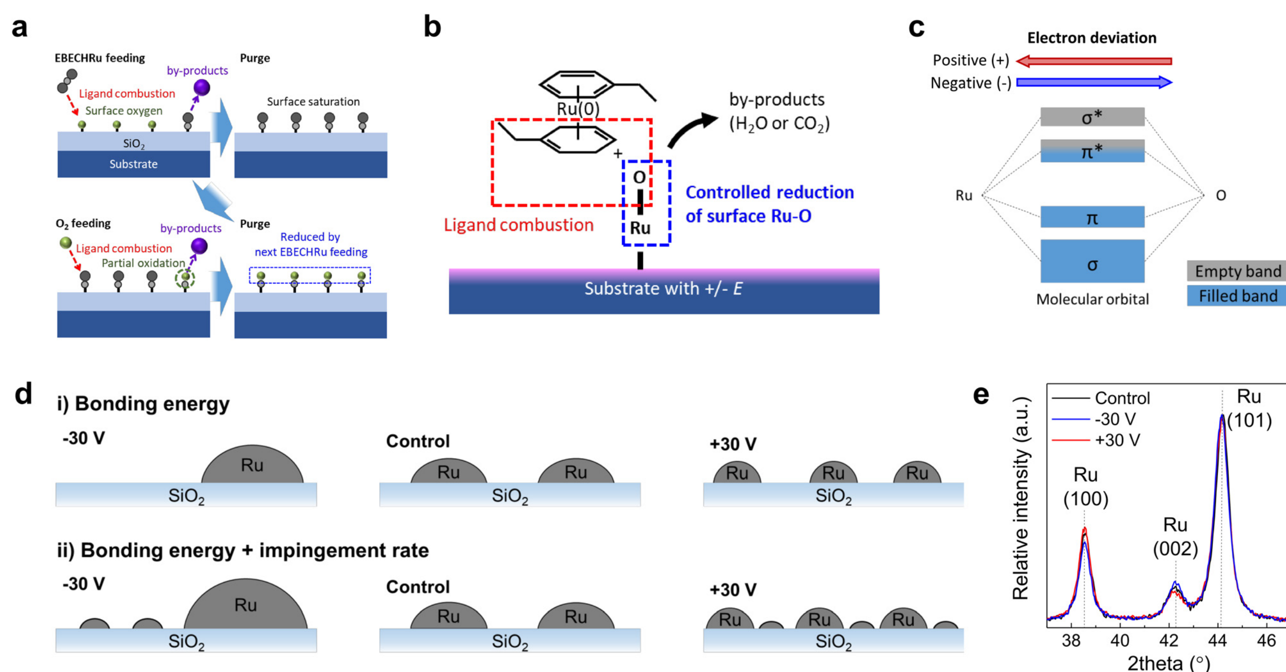

Fig. 2 (a) Schematics of surface reactions in ALD of the Ru film. (b) Surface reaction between a precursor molecule and a surface Ru–O group during the precursor feeding step. The surface reaction rate is affected by the bonding strength of the Ru–O bond. (c) Molecular orbital of the Ru–O bond. The partially filled π* orbital enabled control of the bonding strength by EA-ALD. (d) Schematics of the growth behavior of Ru films grown using control and EA-ALD during the initial growth stage. EA-ALD facilitates nucleation of the film by increasing the impingement rate, and it controls the grain size of the film by modifying the bonding strength of the surface Ru–O bond. (e) GI-XRD patterns of 30 nm-thick Ru films grown using control and EA-ALD.

 This journal is © The Royal Society of Chemistry 2023

Published on 20 February 2023. Downloaded by Hanyang University on 4/15/2024 2:29:21 AM.

incoming precursor molecules on the Ru nuclei. Contrarily, however, the grain size of +30 V Ru is smaller than that of control Ru, because the increased bonding energy of Ru–O prevents the chemical adsorption of incoming precursor molecules on the Ru nuclei, which instead increases the number of Ru nuclei on the SiO_2 substrate through the mobile adsorbed species that did not chemisorb on the Ru nuclei but moved easily onto the SiO_2 surface. Therefore, the grain size of Ru films decreased in the order of −30 V, control, +30 V. In addition to this, considering the enhanced impingement rate of EA-ALD at the same time, both the growth of existing grains and the nucleation of islands on the SiO_2 substrate were facilitated for −30 V Ru. However, for +30 V Ru, the growth of existing grains was suppressed due to the stronger Ru–O bonds, and hence the mobile adsorbed species further contributed to Ru nucleation on the SiO_2 surface. Therefore, resultant nucleation density in +30 V Ru is higher than that of −30 V Ru. Consequently, +30 V Ru has a more uniform and finer microstructure owing to the suppressed growth of existing grains compared with control Ru, but −30 V Ru has a less uniform microstructure because of the facilitated growth of existing grains compared with control Ru. Therefore, the increased surface area of +30 V Ru due to the larger number of nuclei (Fig. 1b) results in a higher deposition rate during the island growth stage compared with −30 V Ru, as shown in Fig. 1c. In following the steady state growth (LBL growth) stage, which is hardly affected by the nucleation behavior and grain size, the enhanced impingement rate of EA-ALD increased the deposition rate compared with control Ru, and modulation of the bonding energy *via* the polarity of the applied electric potential resulted in a higher deposition rate for −30 V Ru compared with +30 V Ru, as shown in Fig. 1c.

Fig. 2e shows the GI-XRD patterns of 30 nm-thick Ru films grown using the control and EA-ALD. All of the Ru films have a hexagonal close packed (HCP) structure. The grain sizes of the Ru films were calculated using the Scherrer equation,[56] and were 13 nm, 12.5 nm and 12 nm for control Ru, −30 V Ru and +30 V Ru, respectively. This is consistent with the discussion above on the increased nucleation density and the change in the surface chemical reaction rate for EA-ALD.[27–30] Meanwhile, the crystal orientation of the film was also affected by EA-ALD. The relative intensity of the (002) plane increased in −30 V Ru compared with control Ru, whereas it decreased in +30 V Ru. The relative intensity of the (100) plane perpendicular to the (002) plane changed in a manner opposite to that of the (002) plane. The (002) plane is the close packed plane in the HCP structure with the lowest surface energy among the crystal planes of the HCP structure.[57,58] Therefore, the (002) plane in the direction of growth is preferred when high energy is provided (*e.g.*, a high process temperature or plasma power).[58–60] The lower surface energy of +30 V Ru due to stronger Ru–O bonds results in a less preferred orientation of the (002) plane. By contrast, the surface energy increased in −30 V Ru due to the weaker Ru–O bonds, enhancing the preferred orientation of the (002) plane in the growth direction.

The microstructure of the Ru films grown on the SiO_2 substrate was observed using TEM and AFM. Fig. 3a shows cross-sectional TEM images of the Ru films grown using the control and EA-ALD with 100 and 200 cycles. The surface roughness and the film continuity were improved in the EA-ALD films compared with the control film. The Ru films with 200 cycles clearly show differences in the grain sizes of the films discussed above. The control Ru and −30 V Ru exhibit a rough surface and an unevenly distributed size of grains compared with +30 V Ru. In addition, the grain size of −30 V Ru is smaller than that of control Ru, on average, but some of the grains are larger than that of control Ru due to the facilitated growth of Ru islands during the initial stage of growth, as mentioned above. Therefore, the surface roughness of −30 V Ru is higher than that of control Ru. The +30 V Ru films exhibit a smooth surface and an even grain size distribution due to the improved nucleation density and suppressed growth of Ru islands during the initial stage of growth. In Fig. 3b, the surface morphology of 30 nm-thick Ru films was confirmed using AFM. The RMS roughness values of the films were 0.9 nm, 1.7 nm and 0.8 nm for control Ru, −30 V Ru, and +30 V Ru, respectively. +30 V Ru and −30 V Ru exhibited a lower and higher roughness than control Ru, respectively, which corresponds to the previous TEM results (Fig. 3a). Grain size distributions on the surface of the Ru films were analyzed based on the AFM images as shown in the overlapping histograms and box charts in Fig. 3b. The average particle sizes, indicated as the square dot in each box chart, were 36 nm, 33 nm and 31 nm for control Ru, −30 V Ru and +30 V Ru, respectively. The upper and lower lines of the box represent the upper and lower quartiles of the data, respectively, and the line between the upper and lower lines represents the median. The range of the box for −30 V Ru is larger than that for control Ru, and the median line is lower for −30 V Ru, which suggests that the grain size of −30 V Ru is

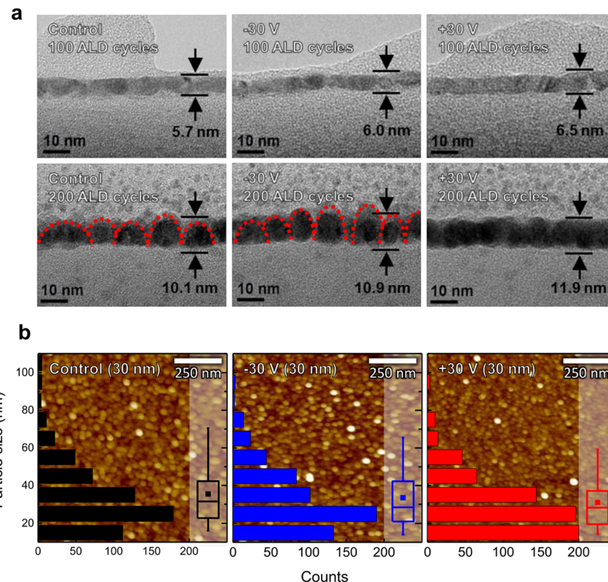

Fig. 3 (a) Cross-sectional TEM images of the Ru films grown using control and EA-ALD with 100 and 200 cycles. (b) AFM images of 30 nm-thick Ru films grown using control and EA-ALD with particle size distribution analysis. The grain size and distribution in the Ru films was crucially modified by EA-ALD.

Published on 20 February 2023. Downloaded by Hanyang University on 4/15/2024 2:29:21 AM.

usually smaller than that of control Ru, although there are also irregularly larger grains. As a result, −30 V Ru is confirmed to have a more dispersed distribution of grain sizes than control Ru. By contrast, for +30 V Ru, the narrow range of the box with a smaller median than for the other films indicates a more uniform grain size distribution. Consequently, the microstructure of the films observed *via* TEM (Fig. 3a) and grain size distribution analyzed using AFM (Fig. 3b) correspond to the proposed film growth model in Fig. 2.

Fig. 4a–c show the TOF-SIMS depth profiles of Ru, O and C, respectively, in 40 nm-thick Ru films grown using control and EA-ALD, and reveal the differences in the chemical structure and residual impurity. Si signals were also included in Fig. 4a–c to indicate the substrate. The differences between the Ru signal profiles in all the films were negligible, while the O and C impurity profiles showed distinct differences for each film. The oxygen impurity concentration was considerably higher for the EA-ALD films compared with control Ru because the decreased grain size increased the area of grain boundaries where the adsorption of oxygen used as a reactant was enhanced. Grain boundaries are preferred sites for the chemical reaction because they are thermodynamically less stable than the grain.[56] The carbon impurity concentration, however, was suppressed in EA-ALD, since these are generated from hydrocarbon ligands of the Ru precursor molecule.[24,25,61,62] This is attributed to the 'cooperative effect', which is described below. Shirazi *et al.* and Maimaiti *et al.* reported that the activation energy of a surface reaction can be reduced when a large number of surface functional groups are present on the surface.[63,64] The lowered activation energy increases the partial pressure of the reaction product,[26] which means the more effective removal of ligands during the ALD reaction. EA-ALD increased the adsorption of precursor molecules and thus the number of surface groups, which enhanced the 'cooperative effect', resulting in a lower carbon impurity concentration in the EA-ALD films compared with control Ru. In addition, the lower carbon concentration of +30 V Ru than −30 V Ru is attributed to an enhanced 'cooperative effect' *via* the higher adsorption rate of precursor molecules in +30 V Ru during the island growth stage, as discussed above (Fig. 1c).

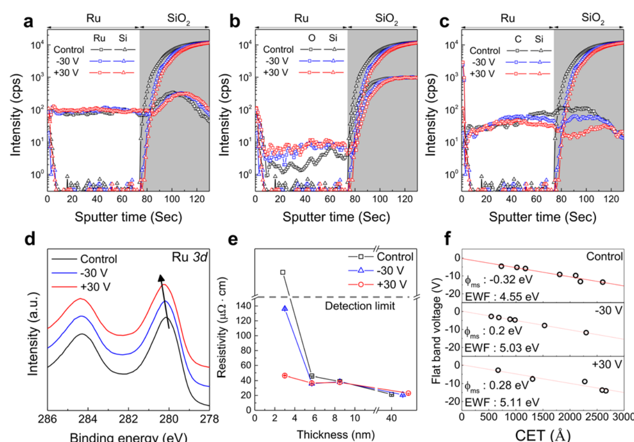

Fig. 4 TOF-SIMS depth profile of (a) Ru, (b) O, and (c) C in 40 nm-thick Ru films grown using control and EA-ALD. The oxygen impurity concentration increased but the carbon impurities decreased in the EA-ALD Ru films. (d) Ru 3d core level spectra of 40 nm-thick Ru films. (e) Resistivities of the Ru films grown using control and EA-ALD as a function of the film thickness. The resistivity of ultrathin (∼3 nm) Ru films became measurable, with values as low as 140 and 40 μΩ cm for −30 V Ru and +30 V Ru, respectively. (f) Effective work function (EWF) of 20 nm-thick Ru films grown on an SiO_2 substrate using control and EA-ALD, where the EWF values are 4.55 eV, 5.03 eV and 5.11 eV for control Ru, −30 V Ru and +30 V Ru, respectively.

Fig. 4d shows the Ru 3d core level spectra of 40 nm-thick Ru films grown using the control and EA-ALD. The surface contamination and native oxide of Ru films was removed by Ar sputtering before XPS analysis. The Ru $3d_{5/2}$ peak is located at the binding energy of 280 eV for control Ru, and is shifted to a higher binding energy for the EA-ALD films. This suggests that the increased oxygen impurities (Fig. 4b) increased Ru–O bonding in the films.[65–67] In addition, the intensity of the O 1s core level spectra directly showed the increased amount of Ru–O bonding in the EA-ALD films (Fig. S3, ESI†), which was obtained with a delicate intensity calibration for quantitative comparison.

The resistivity and the effective work function (EWF) of Ru films grown using control and EA-ALD were measured. The detailed fabrication process of the devices for electrical measurement is provided in Fig. S4, ESI.† Fig. 4e shows the resistivity of the Ru films as a function of the film thickness. The resistivity of 3 nm-thick control Ru was out of the measurable range due to its poor continuity as a result of the low nucleation density. By contrast, the 3 nm-thick −30 V Ru and +30 V Ru exhibited low resistivities of 140 and 40 μΩ cm, respectively, due to the reduced critical thickness from the improved nucleation density. The resistivity of +30 V Ru was lower than that of −30 V Ru due to the better film continuity and smoother surface morphology with more uniform grains. The resistivities of all the films decreased and saturated at ∼20 μΩ cm with increasing film thickness. Fig. 4f shows the EWF of the Ru films as a function of the capacitance equivalent thickness (CET).[12,68–70] The EWF and CET were calculated from the *C–V* curves of the MOS capacitors. The EWF values were 4.55 eV, 5.03 eV, and 5.11 eV for control Ru, −30 V Ru and +30 V Ru, respectively. Since RuO_2 has a higher work function (5.2 eV) than pure Ru (4.8 eV),[7,8] oxygen impurities in the films increased the EWF of the films.[71,72] It should be noted that the resistivities of the EA-ALD films were lower than that of control Ru despite the higher oxygen impurity concentration.

Conclusions

Ru thin films were grown using electric-potential-assisted ALD (EA-ALD). An electric potential is applied to the substrate during the ALD process, which modifies the bonding strength of the surface functional groups and generates an electric field that enhances the impingement rate of precursor molecules. Enhanced the impingement rate increased the nucleation

 This journal is © The Royal Society of Chemistry 2023

Published on 20 February 2023. Downloaded by Hanyang University on 4/15/2024 2:29:21 AM.

density, leading to a reduced critical thickness for the formation of a continuous film and a higher Ru deposition rate. The bonding strength of the surface Ru–O groups decreased with a negative potential and increased with a positive potential, resulting from deviation of the electron density, which affected the adsorption of precursor molecules on the Ru nuclei, determining the grain size and crystal orientation of the Ru films. As a result, EA-ALD with a positive potential resulted in a smoother surface and a more even particle size distribution compared with the control Ru film. The oxygen impurity concentration was increased using EA-ALD because the area of the grain boundaries where oxygen adsorbs easily was increased with the smaller grain size, which increased the effective work function of the Ru films. The carbon impurity concentration decreased because the enhanced surface reaction from the cooperative effect diminished the unreacted residual ligands. Resistivities of 140 and 40 μΩ cm were obtained for ultrathin (∼3 nm) EA-ALD Ru films with negative and positive potentials, respectively, while that of the control Ru film was unmeasurable due to its discontinuity.

Author contributions

Ji Won Han: formal analysis, investigation, methodology, visualization, writing – original draft. Hyun Soo Jin: formal analysis, investigation, methodology, visualization. Yoon Jeong Kim: formal analysis, data curation. Ji Sun Heo: data curation. Woo-Hee Kim: validation, supervision. Ji-Hoon Ahn: validation, supervision. Tae Joo Park: conceptualization, project administration, funding acquisition, supervision, validation, writing – review and editing.

Conflicts of interest

There are no conflicts to declare.

Acknowledgements

This research was supported by the Nano·Material Technology Development Program through the National Research Foundation of Korea (NRF) funded by the Ministry of Science and ICT (NRF-2021M3D1A2043437, 2022M3F3A2A01044952).

References

1 J. Colinge, 1990 IEEE SOS/SOI Technology Conference. Proceedings, October, 1990.
2 S. Y. Kim, B. H. Lee, J. Hur, J. Y. Park, S. B. Jeon, S. W. Lee and Y. K. Choi, *IEEE Electron Device Lett.*, 2018, **39**, 4–7.
3 H. Mertens, 2016 IEEE Symposium on VLSI Technology, Honolulu, Hawaii, USA, June, 2016.
4 D. J. Hagen, J. Connolly, I. M. Povey, S. Rushworth and M. E. Pemble, *Adv. Mater. Interfaces*, 2017, **4**, 1700274.
5 D.-J. Lee, S.-S. Yim, K.-S. Kim, S.-H. Kim and K.-B. Kim, *Electrochem. Solid-State Lett.*, 2008, **11**, K61.
6 P. Schmitt, V. Beladiya, N. Felde, P. Paul, F. Otto, T. Fritz, A. Tünnermann and A. V. Szeghalmi, *Coatings*, 2021, **11**, 173.
7 T.-K. Eom, W. Sari, K.-J. Choi, W.-C. Shin, J. H. Kim, D.-J. Lee, K.-B. Kim, H. Sohn and S.-H. Kim, *Electrochem. Solid-State Lett.*, 2009, **12**, D85.
8 T. E. Hong, S.-H. Choi, S. Yeo, J.-Y. Park, S.-H. Kim, T. Cheon, H. Kim, M.-K. Kim and H. Kim, *ECS J. Solid State Sci. Technol.*, 2012, **2**, P47–P53.
9 S. Y. Mar, J. S. Liang, C. Y. Sun and Y. S. Huang, *Thin Solid Films*, 1994, **238**, 158–162.
10 H. Wang, R. G. Gordon, R. Alvis and R. M. Ulfig, *Chem. Vap. Deposition*, 2009, **15**, 312–319.
11 S. K. Kim, W.-D. Kim, K.-M. Kim, C. S. Hwang and J. Jeong, *Appl. Phys. Lett.*, 2004, **85**, 4112–4114.
12 Y.-S. Suh, H. Lazar, B. Chen, J.-H. Lee and V. Misra, *J. Electrochem. Soc.*, 2005, **152**, F138.
13 M. W. Lane, C. E. Murray, F. R. McFeely, P. M. Vereecken and R. Rosenberg, *Appl. Phys. Lett.*, 2003, **83**, 2330–2332.
14 S.-Y. Bae, J. Mahmood, I.-Y. Jeon and J.-B. Baek, *Nanoscale Horiz.*, 2020, **5**, 43–56.
15 F. Li, G.-F. Han, H.-J. Noh, I. Ahmad, I.-Y. Jeon and J.-B. Baek, *Adv. Mater.*, 2018, **30**, 1803676.
16 R. L. Puurunen and W. Vandervorst, *J. Appl. Phys.*, 2004, **96**, 7686–7695.
17 D. Z. Austin, M. A. Jenkins, D. Allman, S. Hose, D. Price, C. L. Dezelah and J. F. Conley, *Chem. Mater.*, 2017, **29**, 1107–1115.
18 M. A. Alam and M. L. Green, *J. Appl. Phys.*, 2003, **94**, 3403–3413.
19 A. Satta, J. Schuhmacher, C. M. Whelan, W. Vandervorst, S. H. Brongersma, G. P. Beyer, K. Maex, A. Vantomme, M. M. Viitanen, H. H. Brongersma and W. F. A. Besling, *J. Appl. Phys.*, 2002, **92**, 7641–7646.
20 J.-W. Lim, H.-S. Park and S.-W. Kang, *J. Electrochem. Soc.*, 2001, **148**, C403.
21 J.-W. Lim, H.-S. Park and S.-W. Kang, *J. Appl. Phys.*, 2000, **88**, 6327–6331.
22 H. A. Pohl, *J. Appl. Phys.*, 1958, **29**, 1182–1188.
23 H. A. Pohl and J. S. Crane, *Biophys. J.*, 1971, **11**, 711–727.
24 T. Aaltonen, A. Rahtu, M. Ritala and M. Leskela, *Electrochem. Solid-State Lett.*, 2003, 6, C130.
25 T. Aaltonen, M. Ritala, K. Arstila, J. Keinonen and M. Leskelä, *Chem. Vap. Deposition*, 2004, **10**, 215–219.
26 D. R. Gaskell, *Introduction to the Thermodynamics of Materials*, CRC press, Boca Raton, FL, 2012.
27 S. Shaik, D. Mandal and R. Ramanan, *Nat. Chem.*, 2016, **8**, 1091–1098.
28 C. Wang, D. Danovich, H. Chen and S. Shaik, *J. Am. Chem. Soc.*, 2019, **141**, 7122–7136.
29 S. Shaik, D. Danovich, J. Joy, Z. Wang and T. Stuyver, *J. Am. Chem. Soc.*, 2020, **142**, 12551–12562.
30 S. Sowlati-Hashjin and C. F. Matta, *J. Chem. Phys.*, 2013, **139**, 144101.
31 K. P. C. Vollhardt and N. E. Schore, *Organic Chemistry; Palgrave Version: Structure and Function*, Macmillan International Higher Education, London, UK, 2014.

Published on 20 February 2023. Downloaded by Hanyang University on 4/15/2024 2:29:21 AM.

32 R. H. Petrucci, F. G. Herring, C. Bissonnette and J. D. Madura, *General chemistry: principles and modern applications*, Pearson, Carmel, IN, 2017.
33 J. Riga, C. Tenret-Noël, J. J. Pireaux, R. Caudano, J. J. Verbist and Y. Gobillon, *Phys. Scr.*, 1977, **16**, 351–354.
34 D. B. Rogers, R. D. Shannon, A. W. Sleight and J. L. Gillson, *Inorg. Chem.*, 1969, **8**, 841–849.
35 G. Frenking and N. Fröhlich, *Chem. Rev.*, 2000, **100**, 717–774.
36 P. Atkins, P. W. Atkins and J. de Paula, *Atkins' physical chemistry*, Oxford university press, Oxford, UK, 2014.
37 K. Yu, S. Kenta, T. Minoru, U. Hitoshi and K. Hiroshi, *Diamond Relat. Mater.*, 2003, **12**, 560–564.
38 D. K. Biegelsen, R. D. Bringans, J. E. Northrup, M. C. Schabel and L. E. Swartz, *Phys. Rev. B: Condens. Matter Mater. Phys.*, 1993, **47**, 9589–9596.
39 R. Hunger, R. Fritsche, B. Jaeckel, W. Jaegermann, L. J. Webb and N. S. Lewis, *Phys. Rev. B: Condens. Matter Mater. Phys.*, 2005, **72**, 045317.
40 I. Gancarz, G. Poźniak and M. Bryjak, *Eur. Polym. J.*, 1999, **35**, 1419–1428.
41 Z. Fang, J. Yang, Y. Liu, T. Shao and C. Zhang, *IEEE Trans. Plasma Sci.*, 2013, **41**, 1627–1634.
42 L. Liu, X. Liu, L. Kong, M. Wang, P. Hu and D. Wang, *Int. J. Mater. Form.*, 2020, **13**, 885–895.
43 D. Aronov and G. Rosenman, *Surf. Sci.*, 2007, **601**, 5042–5049.
44 S. McDonnell, R. C. Longo, O. Seitz, J. B. Ballard, G. Mordi, D. Dick, J. H. G. Owen, J. N. Randall, J. Kim, Y. J. Chabal, K. Cho and R. M. Wallace, *J. Phys. Chem. C*, 2013, **117**, 20250–20259.
45 F. Grillo, J. Soethoudt, E. A. Marques, L. de Martín, K. Van Dongen, J. R. van Ommen and A. Delabie, *Chem. Mater.*, 2020, **32**, 9560–9572.
46 R. Khan, B. Shong, B. G. Ko, J. K. Lee, H. Lee, J. Y. Park, I.-K. Oh, S. S. Raya, H. M. Hong, K.-B. Chung, E. J. Luber, Y.-S. Kim, C.-H. Lee, W.-H. Kim and H.-B.-R. Lee, *Chem. Mater.*, 2018, **30**, 7603–7610.
47 X. Jiang and S. F. Bent, *J. Phys. Chem. C*, 2009, **113**, 17613–17625.
48 G. N. Parsons and R. D. Clark, *Chem. Mater.*, 2020, **32**, 4920–4953.
49 W.-H. Kim, K. Shin, B. Shong, L. Godet and S. F. Bent, *Chem. Mater.*, 2020, **32**, 9696–9703.
50 P. Wynblatt and N. A. Gjostein, *Prog. Solid State Chem.*, 1975, **9**, 21–58.
51 K. C. Lai, Y. Han, P. Spurgeon, W. Huang, P. A. Thiel, D.-J. Liu and J. W. Evans, *Chem. Rev.*, 2019, **119**, 6670–6768.
52 E. Solano, J. Dendooven, R. K. Ramachandran, K. Van de Kerckhove, T. Dobbelaere, D. Hermida-Merino and C. Detavernier, *Nanoscale*, 2017, **9**, 13159–13170.
53 J. Soethoudt, F. Grillo, E. A. Marques, J. R. van Ommen, Y. Tomczak, L. Nyns, S. Van Elshocht and A. Delabie, *Adv. Mater. Interfaces*, 2018, **5**, 1800870.
54 Z. Li, A. Rahtu and R. G. Gordon, *J. Electrochem. Soc.*, 2006, **153**, C787.
55 F. Grillo, H. Van Bui, J. A. Moulijn, M. T. Kreutzer and J. R. van Ommen, *J. Phys. Chem. Lett.*, 2017, **8**, 975–983.
56 B. D. Cullity, *Elements of X-ray Diffraction*, Addison-Wesley Publishing, Boston, MA, 1956.
57 W. D. Callister, D. G. Rethwisch, A. Blicblau, K. Bruggeman, M. Cortie, J. Long, J. Hart, R. Marceau, M. Ryan and R. Parvizi, *Materials science and engineering: an introduction*, wiley, Hoboken, NJ, 2021.
58 O.-K. Kwon, S.-H. Kwon, H.-S. Park and S.-W. Kang, *Electrochem. Solid-State Lett.*, 2004, **7**, C46.
59 T. Aaltonen, P. Alén, M. Ritala and M. Leskelä, *Chem. Vap. Deposition*, 2003, **9**, 45–49.
60 S.-J. Park, W.-H. Kim, W. J. Maeng, Y. S. Yang, C. G. Park, H. Kim, K.-N. Lee, S.-W. Jung and W. K. Seong, *Thin Solid Films*, 2008, **516**, 7345–7349.
61 A. J. M. Mackus, C. MacIsaac, W.-H. Kim and S. F. Bent, *J. Chem. Phys.*, 2017, **146**, 052802.
62 A. L. Johnson and J. D. Parish, *Organometallic Chemistry*, The Royal Society of Chemistry, Piccadilly, London, UK, vol. 42, 2019, pp. 1–53.
63 M. Shirazi and S. D. Elliott, *Nanoscale*, 2015, **7**, 6311–6318.
64 Y. Maimaiti and S. D. Elliott, *Chem. Mater.*, 2016, **28**, 6282–6295.
65 D. J. Morgan, *Surf. Interface Anal.*, 2015, **47**, 1072–1079.
66 C. L. Bianchi, V. Ragaini and M. G. Cattania, *Mater. Chem. Phys.*, 1991, **29**, 297–306.
67 H. Kim, I. Rabelo de Moraes, G. Tremiliosi-Filho, R. Haasch and A. Wieckowski, *Surf. Sci.*, 2001, **474**, L203–L212.
68 T. Hori, *Gate dielectrics and MOS ULSIs: principles, technologies and applications*, Springer Science & Business Media, Berlin/Heidelberg, DE, 2012.
69 M. Ťapajna, P. Písečny, R. Lupták, K. Hušeková, K. Fröhlich, L. Harmatha, J. C. Hooker, F. Roozeboom and J. Jergel, *Mater. Sci. Semicond. Process.*, 2004, **7**, 271–276.
70 M. Ťapajna, K. Hušeková, J. P. Espinos, L. Harmatha and K. Fröhlich, *Mater. Sci. Semicond. Process.*, 2006, **9**, 969–974.
71 T. Nabatame, K. Segawa, M. Kadoshima, H. Takaba, K. Iwamoto, S. Kimura, Y. Nunoshige, H. Satake, T. Ohishi and A. Toriumi, *Mater. Sci. Semicond. Process.*, 2006, **9**, 975–979.
72 J. K. Schaeffer, L. R. C. Fonseca, S. B. Samavedam, Y. Liang, P. J. Tobin and B. E. White, *Appl. Phys. Lett.*, 2004, **85**, 1826–1828.

 This journal is © The Royal Society of Chemistry 2023